

Modeling energetic particle injections in dynamic pulse fields with varying propagation speeds

Theodore E. Sarris,¹ Xinlin Li,² N. Tsaggas,¹ and N. Paschalidis³

Received 28 May 2001; revised 14 September 2001; accepted 20 October 2001; published 5 March 2002

[1] Dispersionless injections are a ubiquitous characteristic of substorms. They are defined as simultaneous enhancements in the fluxes of electrons and ions of different energies, and they are often observed near or inside geosynchronous orbit. We model dispersionless electron injections by considering the interaction of an earthward propagating electromagnetic pulse with the preexisting electron population. Such simulations have been performed previously [*Li et al.*, 1993, 1998]; however, they assumed a constant propagation velocity for the transient fields. Observations have shown that substorm injections and associated magnetic signatures do not propagate at constant velocities, but rather slow down as they approach the inner magnetosphere. Between 4.5 and 6.6 R_E the injection propagation speeds reach surprisingly low values, of the order of 24 km/s. Nonetheless, the injections still remain dispersionless [*Reeves et al.*, 1996]. In our simulation we vary the pulse speed with the radial distance from the Earth to match the reported propagation speeds and demonstrate that dispersionless injections are achievable under such low propagation speeds. In particular, we simulate the dispersionless injections of 12 February 1991 measured at two radially displaced spacecraft (CRRES and LANL 1990–095), when they were both around local midnight. **INDEX TERMS:** 2753 Magnetospheric Physics: Numerical modeling; 7807 Space Plasma Physics: Charged particle motion and acceleration; 2744 Magnetospheric Physics: Magnetotail; 2788 Magnetospheric Physics: Storms and substorms; **KEYWORDS:** dispersionless, injections, modeling

1. Introduction

[2] Discrete particle injections are typical and common indicators of the onset of a magnetospheric substorm. With the term “injection” we refer to the sudden increase in the particle flux in a detector of finite energy bandwidth [*Kivelson et al.*, 1980]. When such increases appear simultaneously at different energies, the injection is called “dispersionless.” Dispersionless injections at geosynchronous orbit are usually subsequent to a substorm expansion phase and are often observed in a narrow region at or near local midnight [*Belian et al.*, 1978]. The region in which dispersionless injection signatures are observed is referred to as the “injection region”; it is assumed to be that region in which acceleration and/or transport processes are acting locally. Whether or not an injection will appear to be dispersionless depends on the position of the measurement relative to the injection region. When a spacecraft is outside the injection region, it usually observes enhancements of energetic particles that have drifted out of the injection region and are therefore observed with a velocity, or energy, dispersion [*McIlwain*, 1974; *Mauk and Meng*, 1987; *Reeves et al.*, 1996].

[3] In order to explain these energy dispersion features, *McIlwain* [1974] proposed that particles are energized and/or transported very quickly (on timescales faster than ordinary convection times) so that all energies of the distribution fill at one time only an extended region which lies tailward of a sharply defined, nightside, spirallike “injection boundary.” The injection

boundary model suggests that during the injection process a spatial boundary is formed that separates newly injected or energized plasma from the preexisting, undisturbed plasma. This model has been further explored [e.g., *Mauk and McIlwain*, 1974; *Konradi et al.*, 1975; *Mauk and Meng*, 1987]. Another approach [*Moore et al.*, 1981] suggested that a compressionlike wave propagates from the tail regions into the inner magnetospheric regions and heats and transports the plasmas as it goes. Wave heating was used to explain the dispersionless character of some injections.

[4] The propagation of the injection region itself has been a subject of extensive research. The research usually involves more than one set of satellite observations. Observing dispersionless injections at multiple locations is the most secure and interesting way of identifying the direction, velocity, and spatial extent of the particle injection and/or transient field propagation. *Russell and McPherron* [1973], using ATS 1 and OGO 5 data, estimated a propagation speed of 140 km/s between 9 and 6.6 R_E of the compressed magnetic field configuration. They were able to estimate the induced electric field associated with the compressional wave as a few millivolts per meter. Investigation by *Moore et al.* [1981] on substorm injections using measurements from two radially displaced spacecraft (ATS 6 and SCATHA) has shown that dispersionless injections and associated magnetic signatures occur earlier at the outer satellite. They found that the hot plasma propagates earthward in close association with an equally abrupt magnetic field increase at velocities in the range of 10 – 100 km/s. On the basis of their observations they constructed a model known as the convection surge model, which has many qualitative characteristics in common with the current work. *Reeves et al.* [1996], using CRRES, which was in a geosynchronous transfer orbit, and Los Alamos National Laboratory (LANL) energetic particle data at geosynchronous orbit, identified substorms for which dispersionless injections could be observed by both spacecraft. They found that essentially all cases were consistent with an inward/earthward propagation of the substorm injection region.

¹Demokritos University of Thrace, Xanthi, Greece.

²Laboratory for Atmospheric and Space Physics, Boulder, Colorado, USA.

³Applied Physics Laboratory, Johns Hopkins University, Laurel, Maryland, USA.

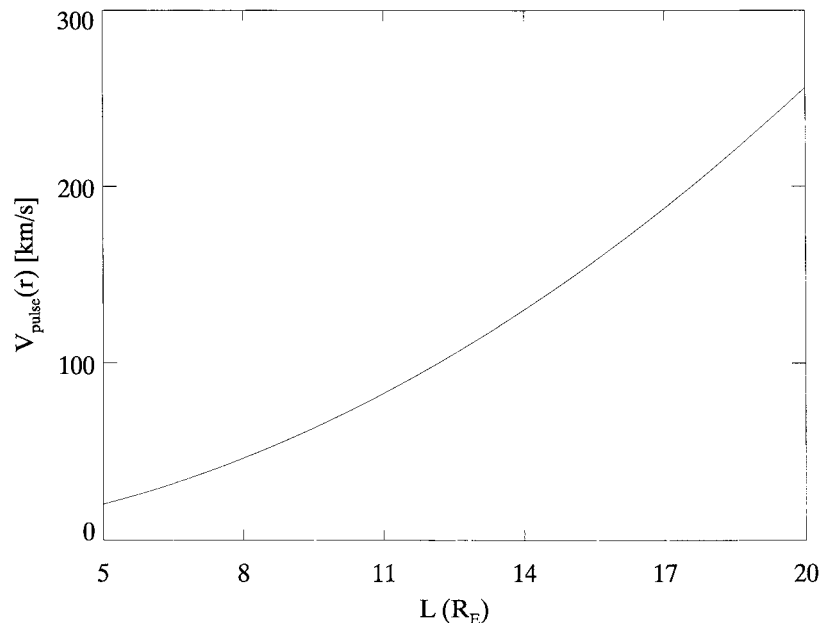


Figure 1. Propagation speed of the earthward pulse as a function of the distance tailward from the Earth. Observations of the propagation speeds of substorm injections at various distances were used to determine the speed function.

They calculated the delay time as a function of the radial separation of the two spacecraft and found that the average propagation speed inside geosynchronous orbit was 24 km/s. It is rather striking that the injections can remain dispersionless at such a low propagation speed since the gradient-B drift velocities of the injected particles are energy dependent and can be comparable or greater than the radial propagation speed of the injections.

[5] The driving force of the injections and the origin of injected particles have also been a subject of research. *Delcourt et al.* [1990] have studied the dynamics of single-particle trajectories in simulations of the substorm expansion phase and have demonstrated enhanced earthward convection of low-latitude plasma in the midtail during that time. Their study focused on ions which may not conserve their magnetic moment under the effect of impulsive fields with significant temporal variations. They demonstrated that this nonadiabatic behavior can lead to dramatic particle acceleration, primarily in the perpendicular direction. *Birn et al.* [1997, 1998], by tracing test particle orbits in the dynamic fields of a three-dimensional MHD simulation of dipolarization in the magnetotail with an imposed inner boundary at $5 R_E$, have found that most energization occurs due to betatron acceleration as particles are transported into a stronger magnetic field region by a time-dependent dawn-dusk electric field. *Li et al.* [1998, 1999] have performed test particle simulations in which an earthward propagating pulse with a constant speed of 100 km/s is superimposed on a background magnetic field and achieved good agreement with observations at geostationary orbit. They conclude that injections are a result of inward propagation of a compressional magnetic field perturbation and its associated electric field and also that the source of energetic particles in dispersionless injections at geosynchronous orbit is more than a few Earth radii tailward. Later, *Zaharia et al.* [2000] used a similar model but a different initial source population (more energetic particles near geostationary orbit), produced good agreement with observations at geostationary orbit, and concluded that the source region is closer to geostationary orbit.

[6] Here we present our simulation of dispersionless injections of electrons measured by two radially displaced satellites at night-

side. The pulse field in our model slows down as it propagates toward the Earth, consistent with the observation.

2. Model

[7] The transient field in our simulation is associated with the dipolarization process in the magnetotail and is modeled as an electromagnetic pulse of localized radial and longitudinal extent propagates earthward. The difference from the previous model of *Li et al.* [1998] is that the pulse propagation velocity now varies with radial distance. The propagation velocity of the peak of the electromagnetic pulse as a function of radial distance is given in Figure 1 which is consistent with observations where the propagation speeds of substorm injections were calculated based on two radially displaced spacecraft [*Russell and McPherron*, 1973; *Moore et al.*, 1981; *Reeves et al.*, 1996].

[8] The electric field is modeled as a time-dependent Gaussian pulse with a purely azimuthal electric field component that decreases away from midnight [*Li et al.*, 1998] and propagates radially inward at a decreasing speed.

[9] In the usual spherical coordinate system (r, θ, ϕ) , where $r = 0$ at the center of the Earth, $\theta = 0^\circ$ defines the equatorial plane and $\phi = 0^\circ$ is at local noon, positive eastward; the electric field is given by

$$\mathbf{E}_\phi = -\hat{e}_\phi E_0 (1 + c_1 \cos(\phi - \phi_0))^p \exp(-\xi^2), \quad (1)$$

where $\xi = [r - r_i + v(r)(t - t_a)]/d$ determines the location of the maximum value of the pulse; $v(r) = a + br$ is the pulse front velocity as a function of radial distance r ; d is the width of the pulse; $c_1 (>0)$ and $p(>0)$ describe the local time dependence of the electric field amplitude, which is largest at ϕ_0 ; $t_a = (c_2 R_E/v_a)(1 - \cos(\phi - \phi_0))$ represents the delay of the pulse from ϕ_0 to other local times; c_2 determines the magnitude of the delay; v_a is the longitudinal propagation speed of the pulse (assumed constant); and r_i is a parameter in the simulation that determines the arrival time of the pulse. In this report we present results with $\phi_0 = 180^\circ$, $E_0 = 4$ mV/m, $c_1 = 1$, $c_2 = 0.5 R_E$, $a = 53.15$ km/s; $b = 0.0093$ s $^{-1}$,

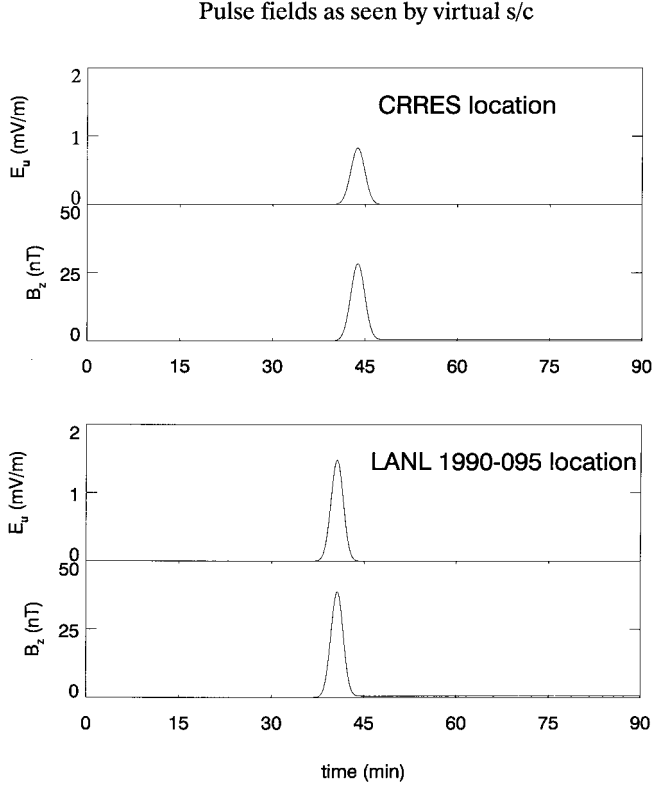


Figure 2. Modeled electric field E_ϕ and magnetic field B_z in the equatorial plane at the two spacecraft locations, as a function of time.

$p = 8$, $v_a = 20$ km/s, $r_i = 100 R_E$, and $d = 4 \times 10^7$ m. The consistent magnetic field of the dipolarization process for a given electric field is obtained from Faraday's law:

$$\frac{\partial \mathbf{B}}{\partial t} = -\nabla \times \mathbf{E}. \quad (2)$$

From (1) and (2), after performing the curl calculation in spherical coordinates and integrating, we obtain the magnetic field:

$$\begin{aligned} \mathbf{B}_0 = & -\hat{e}_\phi E_0 (1 + c_1 \cos(\phi - \phi_0))^p \\ & \times \left(\frac{1 + v'(r)(t - t_a)}{v(r)} \exp(-\xi^2) - \frac{dv'(r)\sqrt{\pi}}{2v(r)^2} \right. \\ & \left. \times (1 + \operatorname{erf}(\xi)) + \frac{d\sqrt{\pi}}{2rv(r)} (1 + \operatorname{erf}(\xi)) \right), \end{aligned} \quad (3)$$

where $\operatorname{erf}(\xi) = \left(\frac{2}{\sqrt{\pi}}\right) \int_0^\xi e^{-x^2} dx$ is the error function.

[10] The magnetic field of the pulse, \mathbf{B}_0 , is superimposed on a background magnetic field, \mathbf{B}_E , which is time dependent. \mathbf{B}_E is modeled as an asymmetrical dipole field with a compressed dayside and a weakened nightside [Li *et al.*, 1998], which has a magnitude of 105 nT at local noon, 75 nT at midnight, and 90 nT at dawn and dusk at geosynchronous orbit. The pulse field and background field satisfy $\mathbf{E}_\phi \cdot (\mathbf{B}_E + \mathbf{B}_0) = 0$ and $\nabla \cdot (\mathbf{B}_E + \mathbf{B}_0) = 0$. In the simulation we consider only equatorially mirroring electrons, which move on average according to the relativistic guiding center equation [Northrop, 1963]:

$$\mathbf{v}_d = c \frac{\mathbf{E} \times \mathbf{B}}{B^2} + \frac{M_r c}{\gamma e} \frac{\mathbf{B} \times \nabla_\perp B}{B^2}, \quad (4)$$

where c is the speed of light in vacuum, e is the electron charge, γ is the relativistic correction factor $(1 - v^2/c^2)^{-1/2}$, $M_r = p_\perp^2 / (2m_0 B)$ is the relativistic adiabatic invariant, p_\perp is the particle's perpendicular momentum, m_0 is the particle rest mass, \mathbf{E} and \mathbf{B} are the vector electric and magnetic fields in the frame of the particle, and ∇_\perp is the gradient perpendicular to the local magnetic field direction. In the energy range that we consider (of the order of hundreds of keV), and for the rate of change both in time and space of the fields in our model, electrons behave adiabatically and equation (4) of the quiding center motion is valid [see also Schultz, 1991; Anderson *et al.*, 1997].

3. Results and Discussion

[11] At the positions of the two radially displaced spacecraft, CRRES and LANL (1990-095), which measured dispersionless injections of electrons on 12 February 1991 [Reeves, 1998], the model fields appear as in Figure 2.

3.1. Single Particles

[12] To demonstrate the effect of the pulse fields outlined in (1) and (3) on charged particles, we trace the orbit of two electrons initially placed at 11 and 8 R_E as shown in Figure 3. Before the pulse's arrival, the electrons' "gradient-B" drift eastward due to the gradient of the background magnetic field. Upon arrival of the incoming pulse, the normal radial gradient of B is abruptly reversed by the pulse field, as seen in Figure 4. This is consistent with the magnetic signatures that are observed to accompany each injection, during which the magnetic perturbation at the equator is usually dominated by an increase in the northward component. As a consequence the eastward gradient-B drift of the electrons stops and even reverses. If viewed globally, this effect can be understood as a propagating current sheet oriented in the east to west direction. At the same time, the electron experiences the pulse electric field and is transported inward due to the " $\mathbf{E} \times \mathbf{B}$ " drift, which is energy independent. As the electron moves inward, the gradient of the background magnetic field begins to dominate and it drifts eastward again.

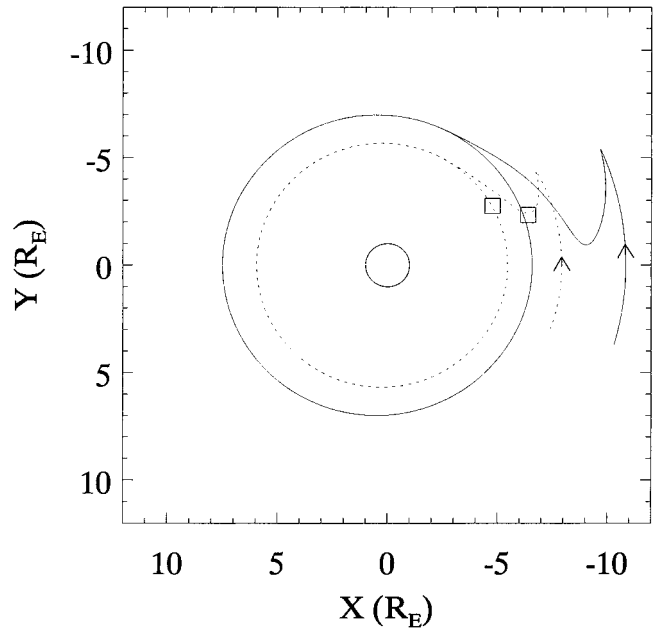


Figure 3. Trajectory of two 90° pitch angle electrons, initially placed in the equatorial plane with $r_0 = 11 R_E$, $W_0 = 20$ keV; and $\phi_0 = 157^\circ$ (solid line), and $r_0 = 8 R_E$, $W_0 = 25$ keV, and $\phi_0 = 155^\circ$ (dotted line).

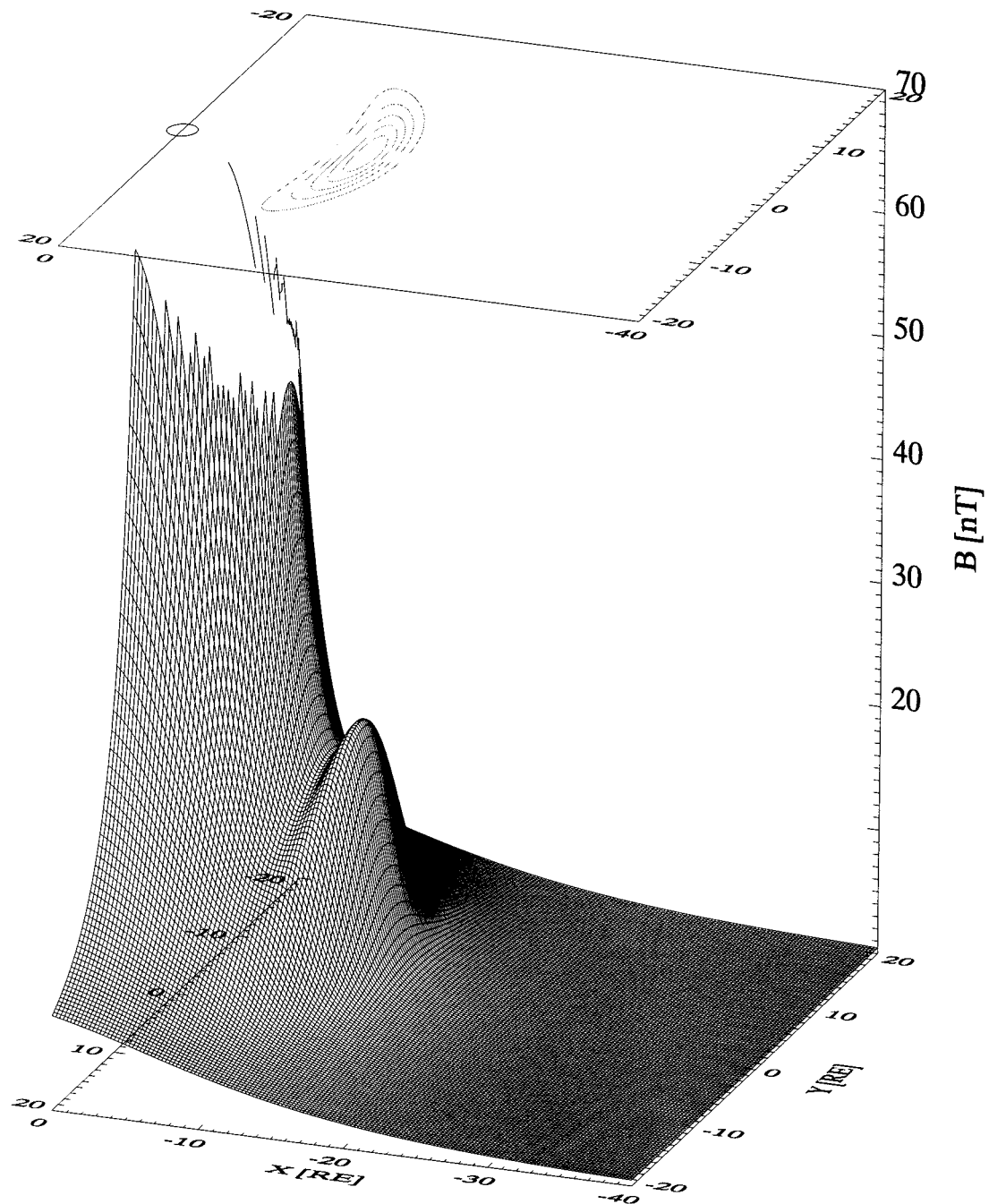


Figure 4. The modeled pulse magnetic field is superimposed on a background time-independent asymmetric magnetic field. Here we show the total magnetic field strength in the equatorial plane, tailward from the Earth, starting from $7 R_E$. The background magnetic field has an inward gradient which is reversed upon arrival of the electromagnetic pulse.

[13] As a result of their inward motion to a stronger background magnetic field, electrons gain energy. If the first adiabatic invariant, M_p , is conserved, which is true for the electrons and perturbation fields in question, the energy gain depends only on the magnetic field at the particle initial and final positions.

3.2. Many Particles

[14] So far we have described the effect of the modeled fields on single particles. In order to compare with satellite observations, we need to turn the individual particle orbits into some-

thing that can be compared with the data, which in this case is a differential particle flux measured by a detector. We construct the simulated electron flux at the virtual spacecraft positions by tracing many electrons and recording their energy, arrival time, radial distance, and initial conditions as they pass by the virtual spacecraft's positions. In the simulation we trace 1,500,000 electrons in the combined fields of the asymmetric dipole field and the modeled pulse field and we record all electrons that come as close as $0.4 R_E$ to the two satellite positions. These electrons were initially distributed randomly in radial distance between 4 and $16 R_E$ and entire local times in the equatorial

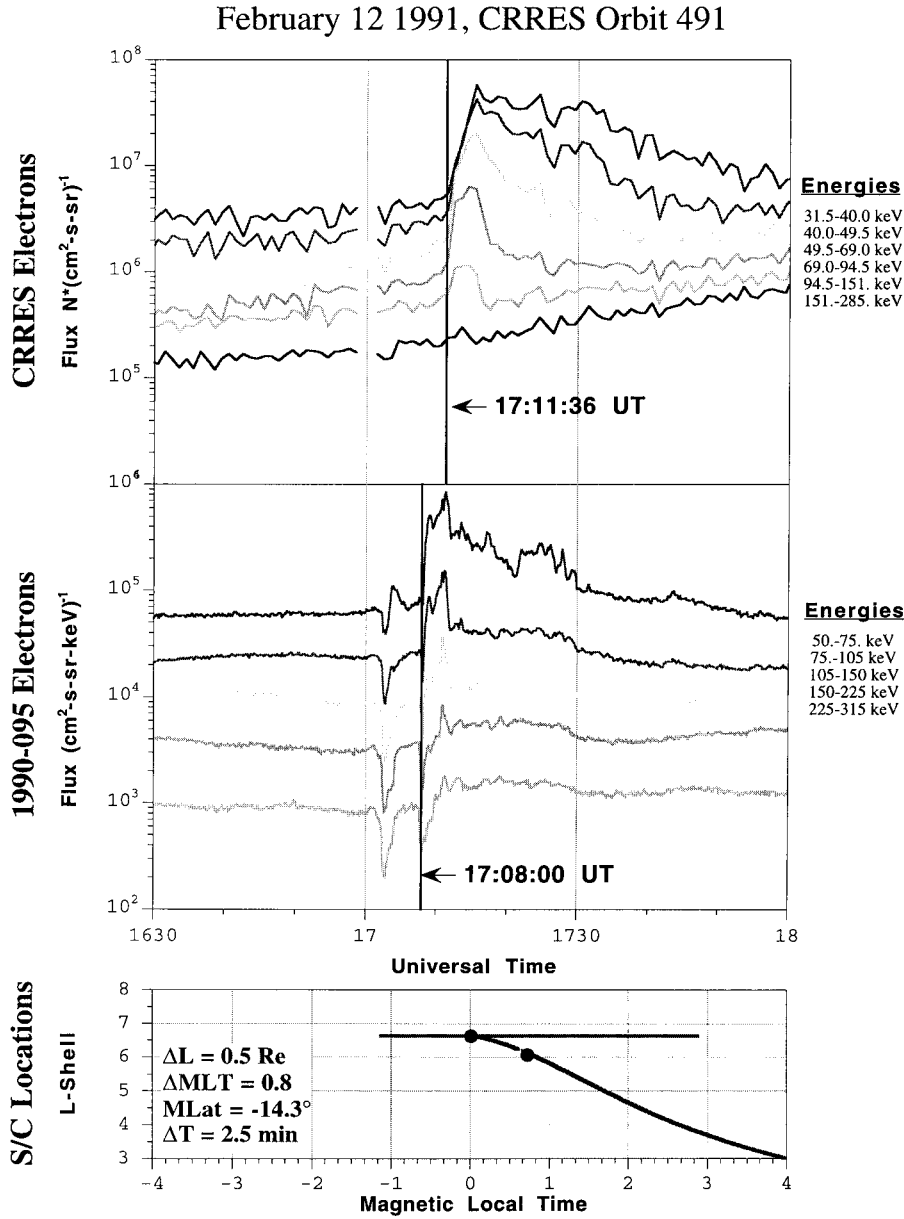


Figure 5. Differential fluxes of electrons from CRRES and LANL 1990-095 observations on 12 February 1991. The spacecraft locations are shown in the bottom panel. LANL satellite was located tailward of CRRES and observed the dispersionless injection (bold line) before CRRES did.

plane. The initial energies start at 6 keV with an increment of 5%, up to 361 keV. Each electron is given a weight based on its initial position and energy to represent its contribution to the initial distribution.

3.3. Particle Weighting

[15] A first weighting factor arises from the bias in the initial spatial distribution: Since we distribute the particles randomly in local time and radial distance, in any finite area $r d\phi dr$ we initially place a finite number of particles, dN , regardless of r . Thus it is clear that an electron in an outer region should represent a larger phase space. To remove the biasing, each particle is given a weight scaling as $(r_i/r_0)^2$, where r_i is the initial radial position of the particle and r_0 is an arbitrary reference distance.

[16] The initial electron distribution in energy is a kappa distribution [Vasyliunas, 1968]:

$$f_w = f_0 \left[1 + \frac{E_i}{(k - \frac{3}{2})E_0} \right]^{-k-1}, \quad (5)$$

with $k = 2.9$, $E_0 = 0.5$ keV, and $f_0 = 256 \text{ km}^{-6} \text{ s}^3$.

[17] The initial radial dependence is set as by Li *et al.* [1998], who use an analytic model to assign a differential flux to each particle:

$$f_r = \left[\frac{(r_0 - a_0)^{nl}}{r_0^{nl}} \right] / \left[\frac{(a_{0d} - a_0)^{nl}}{a_{0d}^{nl}} \right], \quad (6)$$

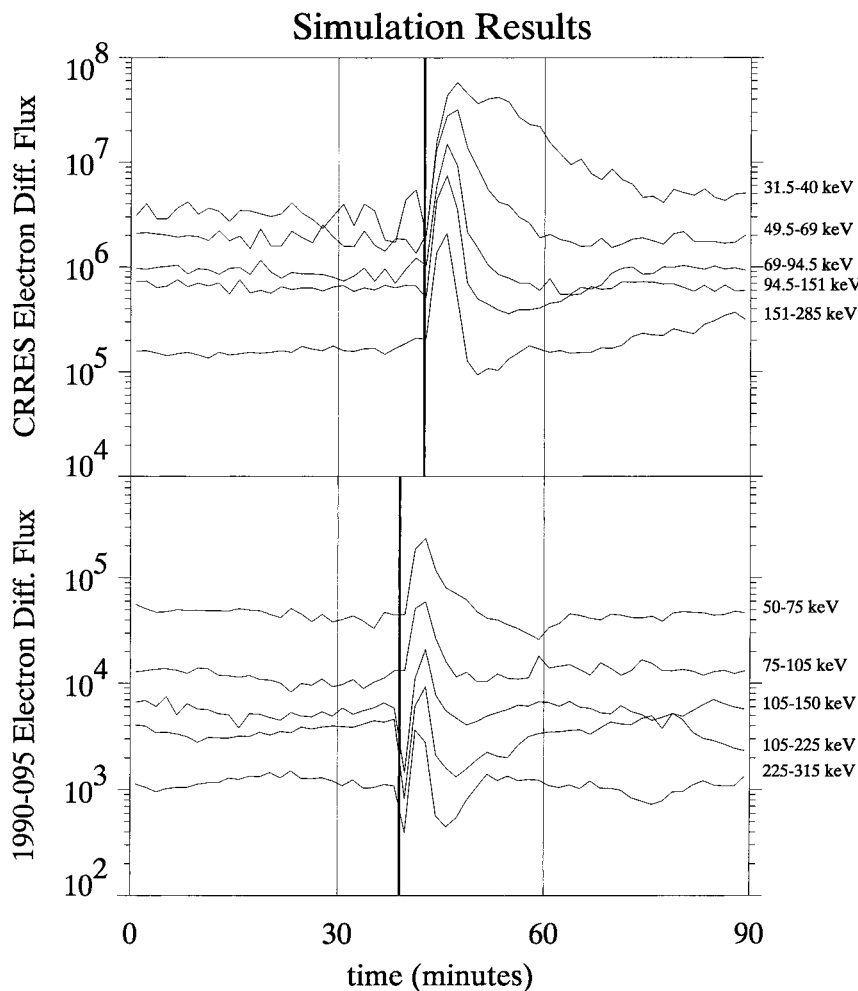


Figure 6. Simulation results. In the simulation we trace electrons in model fields and record them as they pass by two “virtual” satellites, located in the place where CRRES and LANL were at the time of the injections.

with $a_0 = 3$, $nl = 4$, $ml = 10$, $a_{0d} = 6$, and $f_r = f_r \exp(-r_0^2/7.5^2)$ when r_0 is greater than $12 R_E$. We correct for the fact that the real flux is proportional to the particles velocity v by the weighting factor, v/v_d , where v_d is the guiding center velocity.

[18] Finally, we use the factor $\sigma_j(W)$ to account for the energy-dependent geometric factor for the energy channels of the detectors. Here $j = 1, 2, \dots, N$, where N is the number of energy channels for each of the spacecraft. Thus the total weighting factor is

$$Q_{\text{tot}} = \sigma_j f_w f_r \left(\frac{r_i}{r_0} \right)^2 \frac{v_i}{v_0}. \quad (7)$$

3.4. Simulation Versus Observations

[19] We attempt to model the dispersionless injection that was recorded on 12 February 1991 by CRRES and LANL 1990-095, while the two spacecraft were radially displaced as shown in Figure 5. In this event, CRRES, located earthward of LANL 1990-095, observed the injection about 3.5 min later [Reeves *et al.*, 1996]. Both satellites were located around local midnight on the equatorial plane. The injection is clearly seen by the lower-energy channels, where fluxes increase by more than an order of magnitude. The absence of injected particles seen in the highest CRRES energy channel (151–285 keV) and the drop in the high-energy (225–315 keV) LANL electrons at the time of the injection are

typical of such events: Previous observations [Baker *et al.*, 1989; Li *et al.*, 1996] have shown that substorm injections tend to have an upper energy cutoff. Baker *et al.* [1979] showed that only 20% of substorm injections include an increase of electrons with energies greater than ~ 300 keV. This upper energy cutoff is thought to occur because of a lack of source population for >300 keV particles in the near-Earth magnetotail, and because of high-energy particles gradient-curvature B drifting out of the fast-flow region before they can gain appreciable energy or be transported large distances [Reeves *et al.*, 1996].

[20] The simulation as shown in Figure 6 manages to capture the main features of the injection. All energy channels show a simultaneous increase in the electron fluxes, and the injection appears dispersionless to both spacecraft. The time delay from the outer spacecraft to the inner one matches the timing of the injection in the data. Also, the time of the modeled injection matches the pulse arrival times at both spacecraft, as we can see if we compare Figure 2 (model fields) with Figure 6 (simulated electrons), showing that under this model the injected electrons follow the $\mathbf{E} \times \mathbf{B}$ convective velocity. In the simulation we manage to reproduce the injection to the correct magnitude for the lower-energy channels of the two spacecraft. For the higher-energy channels of the virtual spacecraft LANL, we reproduced a temporary drop in the flux, followed by an increase. This drop could be explained as a transport of the local electron population farther inward by the pulse together with a lack of electrons in the particular energy ranges traveling with the pulse.

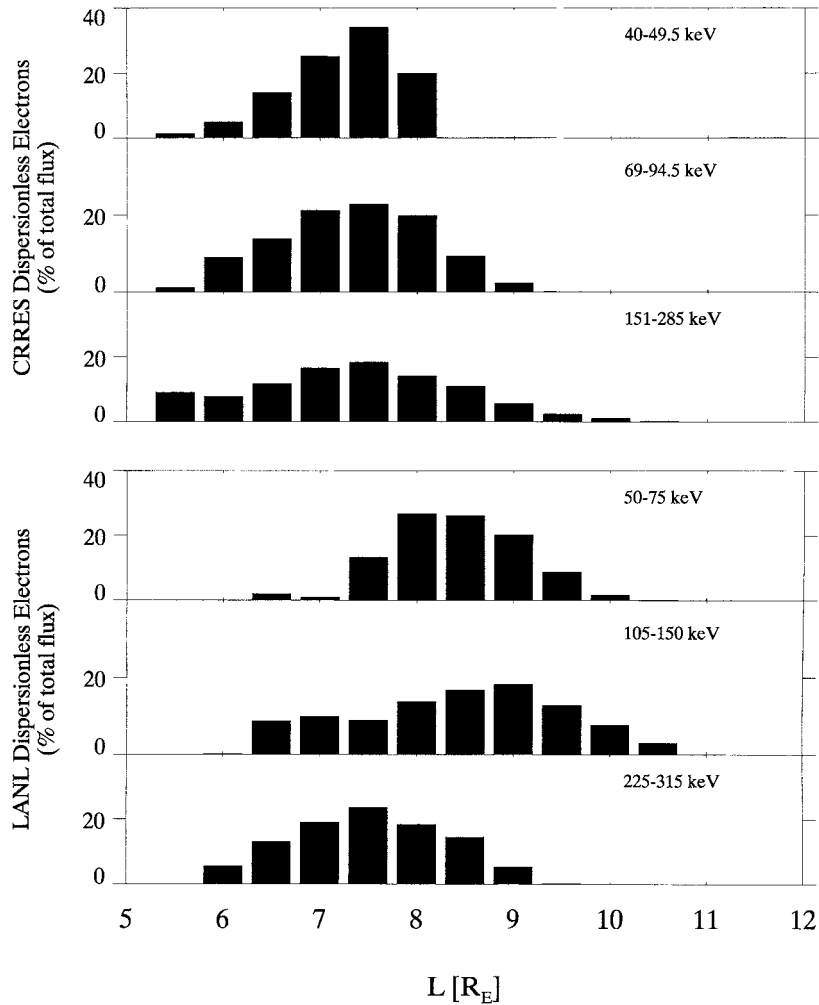


Figure 7. Profile of the initial positions of all the electrons that reach the two spacecraft locations dispersionlessly in the simulation.

[21] The high-energy channels of the simulation show an enhancement in the electron flux, while the corresponding channels of the experimental measurements show a much smaller (or no) enhancement. This is particularly evident in the highest-energy channel of the inner spacecraft, in the upper panels of Figures 5 and 6. We attribute this result to the energy distribution that we use for the source population: As we mentioned, the initial electron distribution in energy is a continuous kappa distribution with $k = 2.9$. A sharper kappa distribution with a larger value for k does, indeed, reduce the electron flux in the high-energy channels; however, it also affects the lower-energy channels and the fluxes measured by the outer spacecraft. A solution to this issue might be an energy distribution with a value for k which varies with radial distance, since, as we will show below, the extent of the region of the source population is different for each energy channel and is also different for the two spacecraft. However, this would require real measurements of the energy profile at various locations at the instance of the dispersionless injection in order for the initial distribution to be realistic.

[22] In Figure 7 we plot a profile of initial positions of electrons that are injected to the two virtual spacecraft positions. We have selected three energy channels for each virtual spacecraft; the top three are for CRRES and the lower three for LANL 1990-95. For a given energy channel each bar represents the percentage of all recorded injected particles that came from the corresponding distance in L . With L here we refer to a contour along which the strength of the unperturbed magnetic field

remains constant. L is identical to radial distance at midnight. Thus, under our asymmetric background magnetic field model, an L value of $6.6 R_E$ corresponds to a radial distance of $6.6 R_E$ at midnight and $7.6 R_E$ at noon. Similarly, L equal to $8 R_E$ corresponds to $8 R_E$ at midnight and $9.8 R_E$ at noon. Bars are plotted every $0.5 R_E$ in L , and the sum of all bars for each energy channel equals one, or 100%.

[23] From this figure we can infer that under this model, the source of electrons injected to inside geosynchronous orbit is from a continuous spatial region, extending to more than a few Earth radii away. The extent of the region is different for each energy channel. On the basis of the above profile of the initial particle positions and taking into account the energy gain of a particle that is adiabatically transported into a region of stronger magnetic field, we would like to comment on the initial energy of particles that contribute to the flux injected to the spacecraft location. The contribution to the flux of the lowest-energy channel (50–75 keV) of the LANL satellite is from electrons of initial energies in the range 12–75 keV, with the lower-energy particles coming from farther away. Similarly for the highest LANL energy channel (225–315 keV) the initial energies are in the range from 90 to 315 keV. The energy distribution that we use for the initial particle population (kappa distribution) is essentially an exponential decrease of particles as energy increases, thus representing the lack of source population for the high-energy particles. This is consistent with what is thought to cause the energy cutoff in the high-energy channels, as discussed earlier.

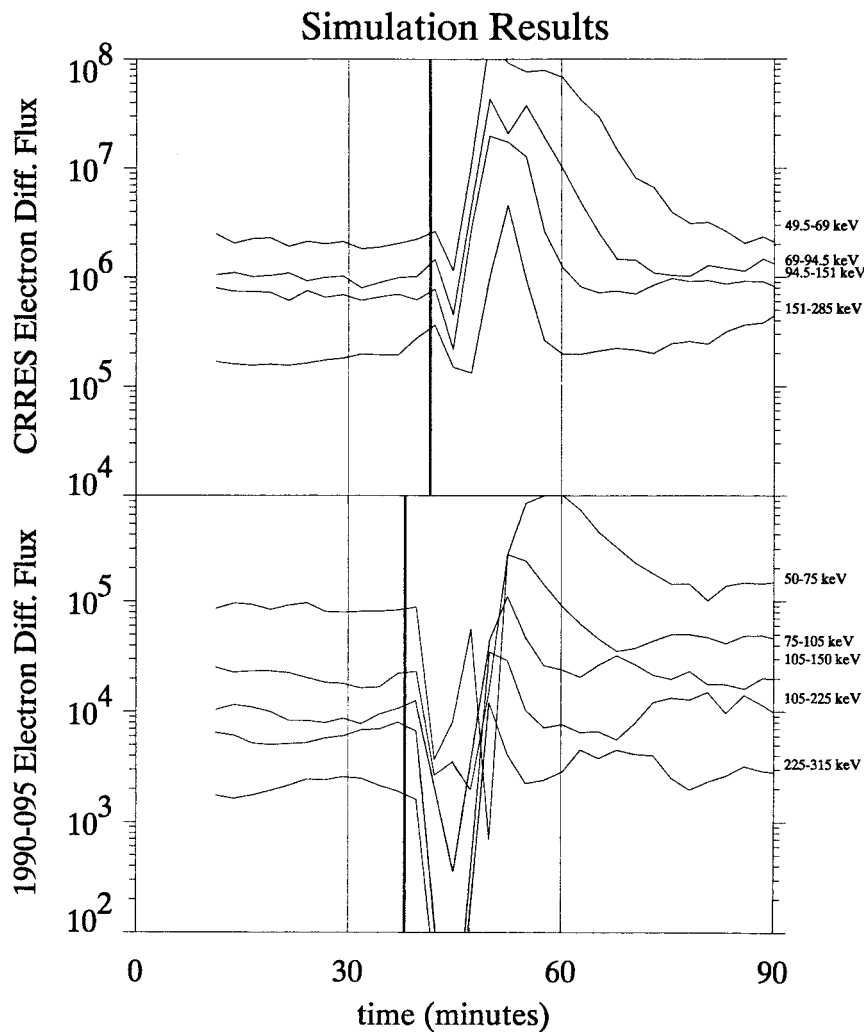


Figure 8. Simulation results for an earthward pulse traveling with a constant speed of 25 km/s.

[24] For the purpose of comparison we carried out another simulation in which the pulse propagates at a constant velocity, using the same particle source population and the same pulse characteristics as mentioned above. The timing of the dispersionless injection in the observations as shown in Figure 5 and the radial separation of the two spacecraft yield a propagation speed of 25 km/s for the injection. We use this constant speed for the pulse in order to maintain the observed time delay between the two spacecraft.

[25] The simulation results for the constant-speed pulse are shown in Figure 8. In this simulation the results are not close to the observation, especially for the outer virtual spacecraft, even though the timing of the injection is reproduced. An explanation for the difference from the simulation results of Figure 6 can be found in (3), which is the expression for the perturbation magnetic field. In this equation the magnitude of the model pulse magnetic field is inversely proportional to the pulse velocity. For the variable-speed case this means that the pulse field amplitude increases as the pulse decelerates. At geosynchronous orbit the average magnetic field from observation is about 70–80 nT (H. Singer, private communication, 2000); the perturbation pulse used in the variable-speed case has a peak value of about 40 nT, which is reasonable compared with the average magnetic field. Tailward from geosynchronous, the pulse amplitude will decrease. In contrast, for the constant-speed pulse the field amplitude remains constant throughout the earthward propagation. The pulse magnetic field for a speed of 25 km/s is unrealistically strong compared

with the background field at and beyond geosynchronous, while it is not necessarily too big with the background field at the location of the inner virtual spacecraft. The pulse magnetic field in the constant speed simulation severely distorts the magnetic field configuration in a nonrealistic way, causing the dropout in the particle population at the LANL 1990-095 site.

[26] As other simulations that we performed have shown, a faster constant-speed pulse does not produce such an unrealistic perturbation field and is able to better reproduce the dispersionless injection at the outer spacecraft site; however, the time delay between the two spacecraft cannot be reproduced. We also experimented with pulses of smaller field amplitudes and we noted that the gradient-B reversal is not as efficient, especially in the location of the inner spacecraft where the background magnetic field is stronger, producing injections of smaller magnitude and with greater dispersion.

[27] From experimenting with various pulse speed functions we have noted that a fast pulse is, in general, less efficient in capturing and transporting particles earthward. From the expression for the radial gradient of the pulse, magnetic field, $\partial \mathbf{B}_\theta / \partial r$, which we give in Appendix A, the inverse power law relation to the pulse speed indicates that we get a larger radial gradient of B_θ for a smaller pulse speed. Thus the gradient-B reversal, which is responsible for capturing the particles under the process that we discussed above, is more effective for slowly propagating pulses. In our model of the decelerating pulse, the dependence of $\partial \mathbf{B}_\theta / \partial r$, on the pulse speed means that we get steeper gradients as the pulse moves radially

inward, in regions where it slows down. Physically, the above process is analogous to a compressional wave propagating inward through a quiet situation; as it is forced to brake in its inward motion, the front of the electromagnetic configuration is compressed and the field gradients become steeper. The above is perhaps another reason why there is a high-energy cutoff: Under our model, if the abundant low-energy particles were to gain sufficient energy to be recorded by a high-energy channel, they would have to be transported inward from farther out, where the transient fields' speed is high and thus less efficient in capturing them.

4. Summary and Conclusions

[28] One of the main questions regarding dispersionless injections involves the azimuthal drift of the particles, which is energy dependent. The injection was usually assumed to be fast so that azimuthal drifts were considered negligible during the injection; a slow injection would allow higher-energy particles to drift over a larger range of local times than lower-energy particles, resulting in dispersion. However, dispersionless injections were still observed for very slow injections [Reeves *et al.*, 1996].

[29] Under the field configuration discussed above, a decelerating transient magnetic field can cancel and/or reverse the magnetic field gradient, thus stopping and/or reversing the electrons' gradient-B drift. Meanwhile the transient electric field results in an $\mathbf{E} \times \mathbf{B}$ drift, which is energy independent, and moves particles toward the Earth, following the pulse propagation front. During this motion the betatron acceleration by the transient fields leads to the energization of charged particles. On the basis of these ideas we constructed the field model and reproduced the main features of dispersionless injections measured by two radially displaced spacecraft with the assumed initial electron distribution. We have shown that under this model, injections can remain dispersionless at surprisingly low propagation speeds.

[30] We have not addressed the question of how the transient field configuration brakes on its earthward motion. The fact is that the earthward transient fields cannot be described as a compressed Alfvén wave, especially inside geosynchronous orbit, because their propagation speeds are much lower than local Alfvén speed. Physically, how the transient field variations propagate from the magnetotail to the inner magnetosphere is still an unresolved issue in magnetospheric physics. On the basis of the test particle simulation, we cannot directly address the mechanisms which generate the transient fields. However, our model is consistent with the idea that an initial perturbation farther out in the magnetotail propagates inward, in the form of high-speed or "bursty bulk" flows, and slows down on the way to the inner magnetosphere region, causing dipolarization and dispersionless injections.

Appendix A: Radial Gradient of the Pulse Magnetic Field

[31] The radial gradient of the pulse magnetic field, which is responsible for the gradient-B reversal discussed above, is calculated from equation (3) of the pulse magnetic field. It is larger for smaller pulse speeds; thus under our model of the decelerating pulse the radial gradient increases and the pulse becomes sharper with inward propagation.

$$\frac{\partial \mathbf{B}_0}{\partial r} = -\hat{e}_r E_0 (1 + c_1 \cos(\phi - \phi_0))^p \times \left[\frac{e^{-\xi^2}}{v(r)^3} \left(2v(r)v'(r) + 2(t - t_a)v'(r)^2 - (t - t_a)v(r)^2 v''(r) \right) \right]$$

$$\begin{aligned} & + \frac{e^{-\xi^2}}{v(r)^3} \left(\frac{2\xi v(r)^2}{d} [1 + (t - t_a)v'(r)]^2 \right) \\ & + \frac{1 + \operatorname{erf}(\xi)}{v(r)^3} \left(\frac{d\sqrt{\pi}}{2} [2v'(r)^2 - v(r)v''(r)] \right) \\ & + \frac{e^{-\xi^2}}{rv(r)} (1 + (t - t_a)v'(r)) + \frac{1 + \operatorname{erf}(\xi)}{rv(r)} \\ & \times \left(\frac{-d\sqrt{\pi}}{2} [1/r + v'(r)/v(r)] \right), \end{aligned} \quad (\text{A1})$$

where $\operatorname{erf}(\xi) = \left(\frac{2}{\sqrt{\pi}} \right) \int_0^\xi e^{-x^2} dx$ is the error function, $\xi = [r - ri + v(r)(t - t_a)]/d$ determines the location of the maximum value of the pulse, and $v(r)$ is the velocity of the front of the pulse as a function of the radial distance r .

[32] **Acknowledgments.** This work was supported by NASA grants NAG 5-9421 and 5-10474 and NSF grants ATM-9909357 and -9901085. The research was conducted during T.E.S.'s visit to LASP. T.E.S. wishes to thank M. Temerin and S. Elkington for useful discussions.

[33] Michel Blanc thanks Geoff Reeves and John Wygant for their assistance in evaluating this paper.

References

- Anderson, B. J., R. B. Decker, N. P. Paschalidis, and T. Sarris, Onset of nonadiabatic particle motion in the near-Earth magnetotail, *J. Geophys. Res.*, *102*, 17,553, 1997.
- Baker, D. N., R. D. Belian, P. R. Higbie, and E. W. Hones, Jr., High-energy magnetospheric protons and their dependence on geomagnetic and interplanetary conditions, *J. Geophys. Res.*, *84*, 7138, 1979.
- Baker, D. N., J. B. Blake, L. B. Callis, R. D. Belian, and T. E. Cayton, Relativistic electrons near geostationary orbit: Evidence for internal magnetospheric acceleration, *Geophys. Res. Lett.*, *16*, 559, 1989.
- Belian, R. D., D. N. Baker, P. R. Higbie, and E. Hones, High-resolution energetic particle measurements at 6.6 R_E , 2, High-energy proton drift echoes, *J. Geophys. Res.*, *83*, 4857, 1978.
- Birn, J., et al., Substorm ion injections: Geosynchronous observations and test particle orbits in three-dimensional dynamic MHD fields, *J. Geophys. Res.*, *102*, 2325, 1997.
- Birn, J., et al., Substorm electron injections: Geosynchronous observations and test particle stimulations, *J. Geophys. Res.*, *103*, 9235, 1998.
- Delcourt, D., J. A. Sauvaud, and A. Pedersen, Dynamics of single-particle orbits during substorm expansion phase, *J. Geophys. Res.*, *95*, 20,853, 1990.
- Kivelson, M. G., S. M. Kaye, and D. J. Southwood, The physics of plasma injection events, in *Dynamics of the Magnetosphere*, edited by S.-I. Akasofu, p. 385, D. Reidel, Norwell Mass., 1980.
- Konradi, A., C. L. Semar, and T. A. Fritz, Substorm-injected protons and electrons and the injection boundary model, *J. Geophys. Res.*, *80*, 543, 1975.
- Li, X., I. Roth, M. Temerin, J. Wygant, M. K. Hudson, and J. B. Blake, Simulation of the prompt energization and transport of radiation particles during the March 23, 1991, SSC, *Geophys. Res. Lett.*, *20*, 2423, 1993.
- Li, X., D. N. Baker, M. Temerin, T. E. Cayton, G. D. Reeves, R. A. Christensen, and J. B. Blake, A source of outer radiation belt electrons: Substorm injections and further accelerations, paper presented at the Chapman Conference on the Earth's Magnetotail: New Perspectives, AGU, Kanzawa, Japan, 5–9 Nov., 1996.
- Li, X., D. N. Baker, M. Temerin, G. D. Reeves, and R. D. Belian, Simulation of dispersionless injections and drift echoes of energetic electrons associated with substorms, *Geophys. Res. Lett.*, *25*, 3763, 1998.
- Li, X., D. N. Baker, M. Temerin, G. D. Reeves, and R. D. Belian, Dispersionless injection simulations explore auroral substorm origins, *Eos Trans. AGU*, *80*, 405, 1999.
- Mauk, B. H., and C. E. McIlwain, Correlation of Kp with the substorm injected plasma boundary, *J. Geophys. Res.*, *79*, 3193, 1974.
- Mauk, B. H., and C.-I. Meng, Plasma injection during substorm, *Phys. Scr.*, *T18*, 128, 1987.
- McIlwain, C. E., Substorm injection boundaries, in *Magnetospheric Phy-*

- sics, edited by B. M. McCormac, p. 143, D. Reidel, Norwell, Mass., 1974.
- Moore, T. E., et al., Propagating substorm injection fronts, *J. Geophys. Res.*, **86**, 6713, 1981.
- Northrop, T. G., *The Adiabatic Motion of Charged Particles*, 29 pp., Wiley-Interscience, New York, 1963.
- Reeves, G. D., New perspectives on substorm injections, in *Proceedings of the Fourth International Conference on Substorms (ICS-4)*, edited by S. Kokubun and Y. Kamide, pp. 785–790, Kluwer Acad., Norwell, Mass., 1998.
- Reeves, G. D., et al., Radial propagation of substorm injections, International Conference on Substorms-3, *Eur. Space Agency Spec. Publ.*, ESA SP-339, 579, 1996.
- Russell, C. T., and R. L. McPherron, The magnetotail and substorms, *Space Sci. Rev.*, **15**, 205, 1973.
- Schultz, M., The magnetosphere, in *Geomagnetism*, edited by J. A. Jacobs, vol. 4, p. 87, Academic, San Diego, Calif., 1991.
- Vasyliunas, D. J., A survey of low-energy electrons in the evening sector of the magnetosphere with OGO 1 and OGO 3, *J. Geophys. Res.*, **73**, 2839, 1968.
- Zaharia, S., C. Z. Cheng, and J. R. Johnson, Particle transport and energization associated with disturbed magnetospheric events, *J. Geophys. Res.*, **105**, 18,741, 2000.

X. Li, Laboratory for Atmospheric and Space Physics, University of Colorado, 1234 Innovation Drive, Boulder, CO, 80303-7814, USA. (lix@paracel.colorado.edu)

N. Paschalidis, Applied Physics Laboratory, Johns Hopkins University, Laurel, MD 20723-6099, USA.

T. E. Sarris and N. Tsaggas, Department of Electrical Engineering, Demokritos University of Thrace, Vas. Sofias 1, 67100, Xanthi, Greece. (tsarris@ee.duth.gr)